Corrosion Science 100 (2015) 267–274

Contents lists available at ScienceDirect

Corrosion Science

journal homepage: www.elsevier.com/locate/corsci

Oxidation behavior of GTD111 Ni-based superalloy at 900 °C in air

J. Brenneman [a], J. Wei [b], Z. Sun [b,*], L. Liu [b], G. Zou [b], Y. Zhou [a,b,**]

[a] Centre for Advanced Materials Joining, University of Waterloo, Waterloo, Ontario N2L 3G1, Canada
[b] Department of Mechanical Engineering, Tsinghua University, Beijing, China

ARTICLE INFO

Article history:
Received 31 March 2015
Received in revised form 15 July 2015
Accepted 31 July 2015
Available online 4 August 2015

Keywords:
A. Nickel
A. Superalloys
B. Modelling studies
B. SEM
C. Interfaces
C. Oxidation

ABSTRACT

The oxidation behavior of GTD111 Ni-based superalloy was investigated at 900 °C from 1 h to 452 h. The detailed oxide structure, from the top surface down to the base material, was clarified by modelling studies as Ni–Ti oxides, Cr–Ti oxides, Cr_2O_3 oxide band, Ni–W–Ta oxide and finally a blocky Al_2O_3 region. Internal oxide Al_2O_3 was discontinuous, Cr_2O_3 oxide dense band provided the most protection against further oxidation. Cracking and spalling of the outer oxides scale results in the nitrogen penetration into the inner oxides scale, and inner nitridation to form TiN occurs. Additionally, the oxidation mechanism was discussed by a model.

1. Introduction

Ni-based superalloys are widely used in the manufacture of aerofoil components such as blades and nozzle guide vanes that operate in the hot sections of advanced gas turbine engines [1–3], due to their good high temperature mechanical properties. These superalloys do not possess adequate oxidation resistance in their service environment, especially at damaged areas where the bare metal is exposed to the oxygen-containing atmosphere. Continual oxidation of the moving crack tip can accelerate the crack's propagation through the component, resulting in shorter service life, especially under thermal cycling conditions. Therefore high oxidation is a main cause, or at least a strong contributor, to the failure of hot-section turbine blades [4].

Characteristics of the oxide films formed on an alloy, including chemical composition, microstructure and thickness, et al., determine the protect ability of the oxide film and thus play a crucial role in the corrosion behavior [5]. Presently, the oxidation structure at high temperature of superalloys has been extensively studied [6–15], as shown in Table 1. The oxidation resistance of Ni-based superalloys at high temperature is achieved by additions of Al and Cr, which preferentially oxidize to form dense, protective oxide films and to slow down the overall oxidation process [8]. It has been found that NiO and Cr_2O_3 are the main oxides formed during oxidation at 700–900 °C of Inconel600 alloy and only NiO has been formed at 600 °C [6]. The oxidation microstructure of Ni-based superalloy at more than 700 °C can be divided into three layers. The outer layer mainly composed Cr_2O_3 and/or NiO, and the inner layer was identified as α-Al_2O_3. The multiphase complex middle layer contained Ti, Ta oxides and some spinel phases, such as $NiCr_2O_4$, $CrTaO_4$, and $NiTa_2O_6$. In all superalloys, a γ'-free layer has been observed underneath the bottom oxide layer, due to element depletion in the oxidation process.

GTD111 was a General Electric (GE) proprietary alloy used for first-stage hot-section turbine blades in the mid-1970s [16]. It is superior to Inconel738 in low-cycle fatigue strength, rupture strength and hot corrosion resistance in the equiaxed form. Trexler et al. results [17] for oxidation tests showed that the oxide structure of GTD111 DS was simply described as $Cr_2O_3 + TiO_2 + Al_2O_3$. The aim of this work is to provide more detailed analysis of distinct oxide regions in GTD111 Ni-based superalloy at 900 °C, as well as the oxidation sequence and mechanism. Note that 900 °C is a typical material surface temperature of turbine blades in stationary gas turbines.

2. Experimental methods

The substrate chosen for this study was a polycrystalline Ni-based superalloy (GTD111, supplied by General Electric Co.,

* Corresponding author: Fax: +86 10 62773862.
** Corresponding author at: Centre for Advanced Materials Joining, University of Waterloo, Waterloo,Ontario N2L 3G1, Canada. Fax: +1 519 885 5862.
E-mail addresses: sunzhg@tsinghua.edu.cn (Z. Sun), nzhou@uwaterloo.ca (Y. Zhou).

http://dx.doi.org/10.1016/j.corsci.2015.07.031
0010-938X/

Table 1
Oxide structure of superalloys in references.

Alloy	Temperature (°C)	Time (h)	Environment	Oxide structure	Reference
Inconel600	600	24	0–19% absolute humidity	NiO	6
	700–900	24		$NiO + Cr_2O_3$	
Rene95	1000	100	Air	$NiO + NiCr_2O_4 + Cr_2O_3$ + oxygen affected zone	7
Prepared alloy	850	300–360	Air	$NiCr_2O_4 + Cr_2O_3 + Al_2O_3$	8
	1000			$NiCr_2O_4 + Al_2O_3$	
TMS82+	800	200	Air + 15% H_2O	$(Ni,Co)O + [NiCr_2O_4 + Cr_2O_3] + Al_2O_3$	9,10
	900		Air + 15% H_2O	$(Ni,Co)O + [NiCr_2O_4 + (Cr,Al)TaO_4 + Cr_2O_3] + [Al_2O_3 + (Ni,Co)Al_2O_4]$	
DD32	900	500	Air	$(NiO + CoO) + (CrTaO4 + NiCr_2O_4) + Al_2O_3$	11
Rene′N5	980–1000	50	Air	$(NiO + Co_3O_4)$ + a multiphase interlayer + Al_2O_3	12,13
PWA1483	950	120		$(NiO + TiO_2) + Cr_2O_3 + Al_2O_3$	14
SCA425+	980	25	Air	$Cr_2O_3 + Ta_2O_5 + [Ni(Cr,Al)\ 2O4 + Ta_2O_5] + Al_2O_3$	12
SCA425+	900	100	Flowing air	$Cr_2O_3 + Ta_2O_5 + Al_2O_3$	14
	1000	100	Flowing air	$Cr_2O_3 + NiTa2O6 + Al_2O_3$	
GTD111	760–1038	100	Dry air	$Cr_2O_3 + TiO_2 + Al_2O_3$	17

Table 2
Composition of the GTD111 alloy used in this study (wt.%).

Cr	Co	Al	Ti	W	Mo	Fe	Ta	C	B	Ni
13.7–14.3	9.0–10.0	2.8–3.2	4.7–5.1	3.5–4.1	1.3–1.7	0.2–0.25	2.5–3.1	0.08–0.12	0.01–0.02	Bal.

American), used for first-stage hot-section turbine blades. The nominal composition of this alloy is shown in Table 2. The incipient melting temperature of GTD111 is considered as 1250 °C. GTD111 in the standard heat treatment condition consists of duplex gamma prime (primary and secondary) precipitates evenly distributed within an FCC gamma matrix. All coupons were cut into 15 mm × 12 mm × 9 mm blocks using Wire Electro-Discharge Machining (EDM) at Excel Wire EDM, Inc.

The surfaces of the samples were polished with SiC abrasive paper to 800# and cleaned ultrasonically with acetone for 10 min before oxidation. Oxidation tests were carried out using an electric air furnace in the ambient air. Coupons were placed in an alumina crucible to oxidize for 1 h, 4 h, 96 h, 144 h, 192 h, 260 h, 308 h and 452 h at 900 °C, respectively, and then rapidly cooled to room temperature. This temperature was chosen to simulate the temperature experienced inside the hot-section of an industrial gas turbine. The furnace temperature was increased at a rate of 25 °C/min up to 400 °C, 10 °C/min up to 750 °C, and 5 °C/min up to 900 °C.

All analyzed samples were ground to a final stage of 1200-grit SiC paper and rinsed with water and ethanol. Etching was only necessary for analysis via optical microscopy (OM, Olympus BX15 M). The samples were immersed in the etchant (10 g H_2SO_4–5H_2O and 50 mL HCl to 50 mL distilled water) for approximately 45 s and then rinsed with water and ethanol. Scanning electron microscopy

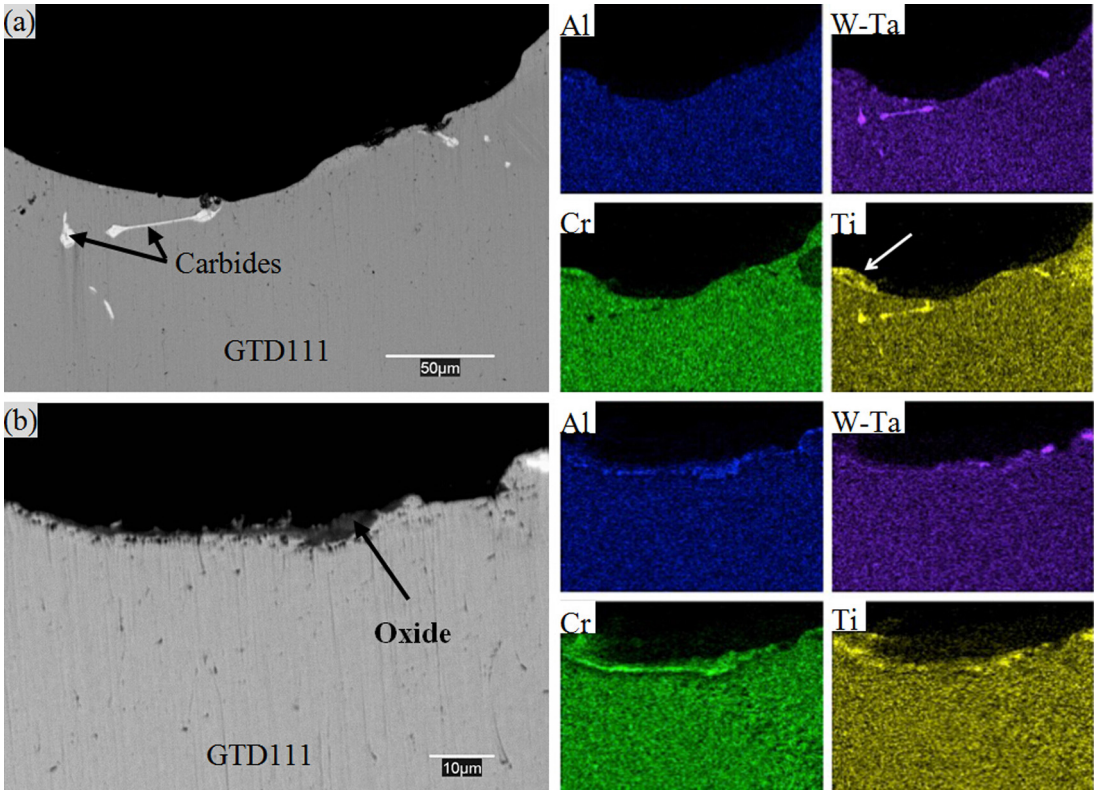

Fig. 1. Microstructure images and EDS mapping results of GTD111 oxidized at 900 °C for (a) 1 h and (b) 4 h.

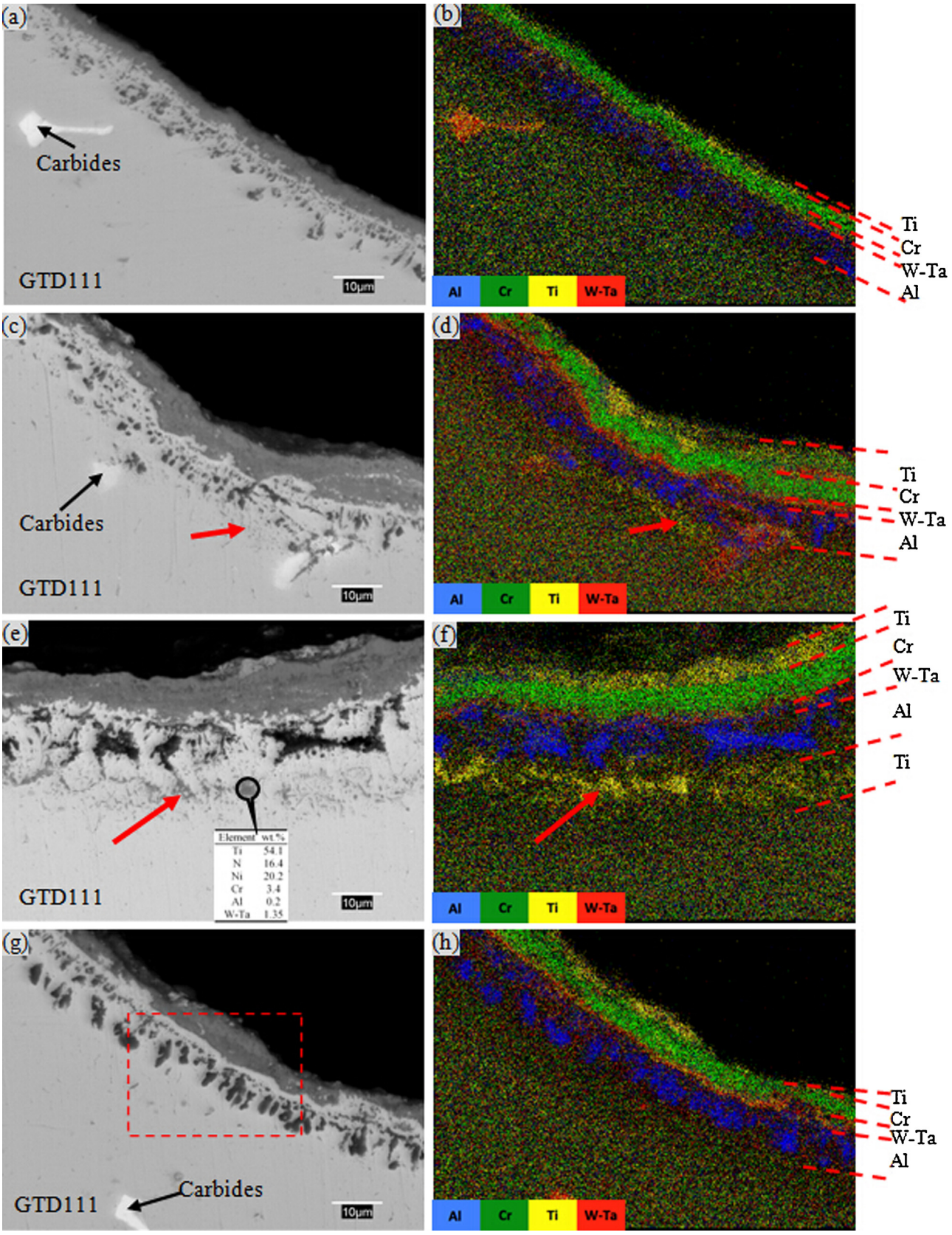

Fig. 2. Microstructure images and element map overlays of samples oxidized for (a, b) 96 h, (c), (d) 192 h, (e), (f) 308 h, and (g), (h) 452 h. The general structure from the top surface down to the base material consists of a gray band rich in Cr (green), a thin white layer rich in W–Ta (red), and dark, isolated, blocky phases rich in Al (blue). Ti (yellow) mostly concentrates above and within the very top portion of the surface, however several TiN particles form below the Al-rich region for 192 h and 308 h oxidation. (For interpretation of the references to color in this figure legend, the reader is referred to the web version of this article.)

(SEM) was performed on a LEO 440 SEM equipped with a Quartz Xone EDX detector. Rigaku Micro-Area X-ray diffraction (XRD) was used to analyze the types of oxide present on the surface of oxidized samples.

3. Results and discussion

3.1. Characterization of the oxidation layer structure

Fig. 1 shows the microstructure and EDS mapping results of GTD111 specimens that had been oxidized at 900 °C for 1 h and 4 h. As shown in Fig. 1a, the 1 h sample exhibited no obvious signs of oxidation, but the Ti element map showed concentrations in some region, and so the first-formed oxide might be that of Ti. Other oxides at the surface seemed to appear in the sample oxidized for 4 h, shown in Fig. 1b, in which bands of concentration were seen in Al and Cr element maps besides Ti. It could therefore be suggested that Al and Cr elements followed Ti to oxidize at 900 °C. The bright blocky phases were indented as carbides rich in W–Ta and Ti, marked in Fig. 1a. The more carbide accumulates at the metal surface the faster the oxide scale will grow [14]. At such times, the extent of oxidation observed was quite low, and the oxides of Al, Ti and Cr were not easily differentiated on the sample. A distinct and stable oxidized structure could not be observed on GTD111 surface until oxidized for 96 h.

Fig. 2 shows the microstructure images and overlaid element maps of samples oxidized for 96–452 h at 900 °C. Very distinct regions of oxide growth were observed after oxidation. Overlaid element maps show the distributions of Al (blue), Ti (yellow), Cr (green), and W–Ta (red) after each oxidation time in Fig. 2. Dark, isolated, blocky phases were found within the sample, above which was a thin white layer, followed by a gray band on the surface in Fig. 2a. This general pattern remained for all oxidation times, and only minor differences were observed as will be discussed later in Fig. 2c, e and g. Contrasting the microstructure with the corresponding overlaid element map, the oxidation process had caused the oxides of Al, Cr, Ti, W and Ta to form at different levels within the sample.

The dark blocky regions (shown as blue color in Fig. 2b) were the deepest-formed oxides and rich in Al. The blue blocky Al-rich region grouped together in a thick, discontinuous region close to the unoxidised base metal with the oxidation time increasing in Fig. 2g and h. However, a continuous aluminum oxide layer was not formed in this oxidation process, for the content of Al in GTD111 (2.8–3.2 wt.%) was less than the threshold (at least 5–7 wt.% Al) at 900 °C [8,15,18]. When the oxidation temperature increased to 1100 °C, Cr_2O_3 oxide changed to gaseous CrO_3 and a continuous Al_2O_3 layer formed as the outer oxide, and acted the most protection against oxidation [19].

A thin W–Ta rich oxide layer (red region) was clearly identified between Cr and Al rich oxide (green and blue region), which agreed with a finding from Sato et al., who observed the formation of a layer rich in Ni and Ta between the chromia and alumina regions [12–13,15]. Trexler et al. [17] provided no details on the "inner oxide layer" of GTD111 and only stated it was high in Ni and Al. The current study has identified that the region high in Ni of the "inner oxide layer" in fact contains W and Ta elements with a thin band distribution. It seemed to be an increasing concentration of Ti (yellow) in the W–Ta (red) rich oxide layer respect to the increasing oxidation time, as shown in Fig. 2b, d, f and h.

A continuous band of Cr rich oxide (green region shown in Fig. 2b) formed even for 96 h oxidation, which would provide the most protection against further oxidation for this alloy. This has been previously observed in alloys with Cr additions of more than 5 wt.% [20]. While the green Cr-rich region appeared to get thicker and be a very dense, continuous oxide layer from 96 h to 452 h of oxidation.

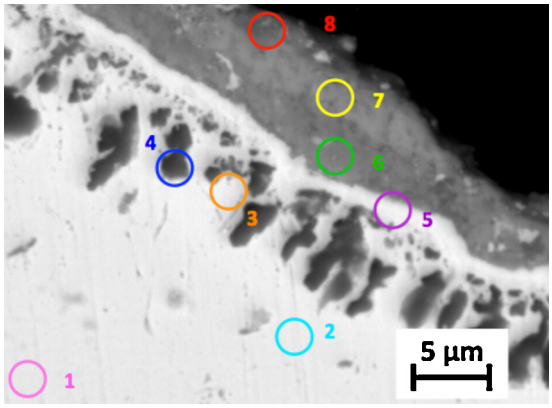

Fig. 3. Magnified BSE image of dashed area in Fig. 2g showing the oxide structure observed for 452 h, with distinct regions numbered. Chemical compositions of each region are listed in Table 3.

After the initial formation of Al and Cr oxides, Ni and Ti could continue to migrate through these regions to form oxide compounds on the surface. Therefore, Ti element (yellow) mostly concentrated on the above and within the very top portion of the surface, whereas Cr concentrations were observed below this Ti region. And also, the exterior regions, found to be rich in Ti (yellow), showed a large variation in thickness and presence with respect to oxidation time, as their weak, porous nature has resulted in their spallation from the surface of the oxidized component [21,22]. It was interesting to observe that Ti concentrations below the Al-rich region changed with the increasing oxidation time. These light gray Ti-rich particles could be identified as TiN by EDS testing (Fig. 2e), not as Ti oxide.

EDS analysis is performed at each region of the numbered circles sampled in Fig. 3, and the results are summarized in Table 3. Although regions 2 and 3 were analyzed as different regions, they have similar in composition, in which the contents of Al, Ti and Cr were lower than that of the base metal (region 1). It is obviously resulted from the diffusions of Al, Ti and Cr driven by their own concentration gradients induced by the oxidation reaction. Region 4, blocky dark phase was identified as Al_2O_3 phase. A thin, continuous band (region 5) was mainly composed of Ni, W and Ta, containing 9.3 wt.% Ti. Region 6 corresponding to the green band in overlaid element maps can be identified as Cr_2O_3 phase. Regions 7 and 8 corresponding to the exterior regions were all rich in Ti, but Cr in region 7 beside the Cr_2O_3 band was much higher than region 8 located at the exterior surface.

XRD analysis was performed on the surface of the sample to determine the outermost oxides present at each oxidation time. Therefore the actual oxide compounds observed could not be identified, but it was clear that only the oxides of Ni–Ti, Cr–Ti and Ni–Cr spinel phases were present at the surfaces of oxidized samples from 96 to 452 h as shown in Fig. 4. NiO was observed on the surface for 308 h oxidation, and then disappeared on the sample of 452 h oxidation, which was contributed to the spallation of NiO and the formation reaction of spinel phases as follows [12].

$$NiO + Cr_2O_3 = NiCr_2O_4 \quad (1)$$

$$5NiO + TiO_2 = Ni_5TiO_7 \quad (2)$$

Fig. 5 shows a schematic model of the general oxidized structure seen on GTD111 in the range of 96–452 h at 900 °C. This schematic model provides much more detail on the oxide structure of GTD111

Table 3
Average concentrations of the main oxidizing elements present in each distinct region (wt.%).

Region	Al	Ti	Cr	Ni	W–Ta	O	Description
1	3.5	4.6	12.2	62.7	6.7	0.0	Base metal
2	1.7	2.2	8.7	68.0	6.2	0.0	Lower Depleted
3	1.4	0.4	5.5	69.3	7.5	2.2	Upper Depleted
4	33.7	1.5	2.2	17.3	2.1	40.0	Al-rich
5	1.7	9.3	7.3	34.6	19.4	20.9	Ni–W–Ta-rich
6	1.2	4.6	47.8	3.1	2.1	39.1	Cr-rich
7	2.2	10.4	18.6	16.1	1.6	34.5	Cr–Ti-rich
8	2.1	9.0	6.6	25.3	3.9	27.5	Ni–Ti-rich

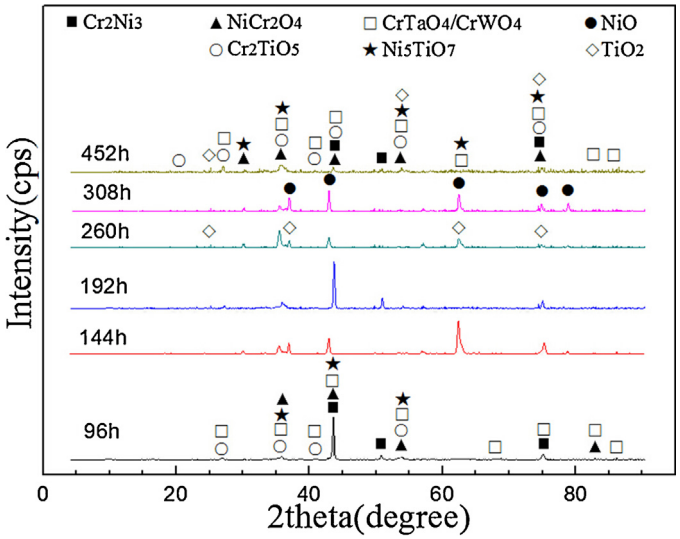

Fig. 4. XRD plots of the peaks observed after 96–452 h oxidation at 900 °C. 2θ peaks of corresponding to Cr_2Ni_3, NiO, TiO_2, $NiCr_2O_4$, Ni_5TiO_7, Cr_2TiO_5, and $CrTaO_4/CrWO_4$ are detected on the outermost oxide layer.

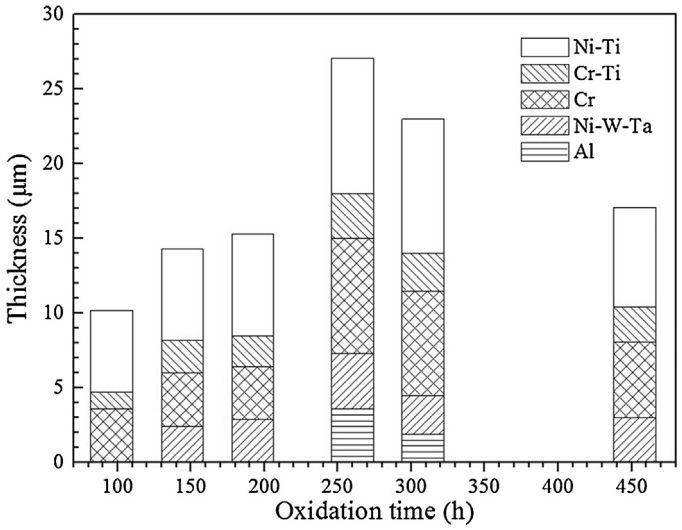

Fig. 6. Thickness profiles of different oxide layers for 96–452 h oxidation at 900 °C. Cr, Cr–Ti and Ni–Ti oxides could have the largest effect on the overall oxide thickness.

than what has been noted in previous publications. In all cases, the deepest-forming oxide islands were rich in Al, and were surrounded by a gamma prime phase depletion region, unoxidised base metal reaching even deeper into the bulk material. Observed above this Al region was a thin, continuous band of Ni–W–Ta oxide, followed by a thicker, continuous and very dense band of Cr oxide. And a thin band of Cr–Ti oxide, inconsistent in thickness, formed atop the Cr-rich band. Finally, outermost regions rich in Ni and Ti were observed at some oxidation times, but their presence was very sporadic, and these weak oxide regions may have spalled from the surface, due to the differences in CTE between different oxide regions during cooling or the process of grinding.

3.2. Oxides thickness profiles analysis

The thickness of different oxides layers changed with oxidation time, as shown in Fig. 6. The thickness fluctuations of Cr, Cr–Ti and Ni–Ti oxides (the outer oxides) were larger than that of Al and Ni–W–Ta oxides (the inner oxides) with respect to time, and determined the change trend of the overall thickness. The upper exterior region (Ni–Ti and Ni–Ti oxide), especially, exhibited large fluctuations, and was only present at times of 260 and 308 h, where the overall oxide thickness was observed to be the greatest. It can be stated that their presence or absence could have the largest effect on the overall oxide thickness.

The overall oxides thickness increased with oxidation time from 96 h to 260 h, for the elements diffusions from the substrate. How-

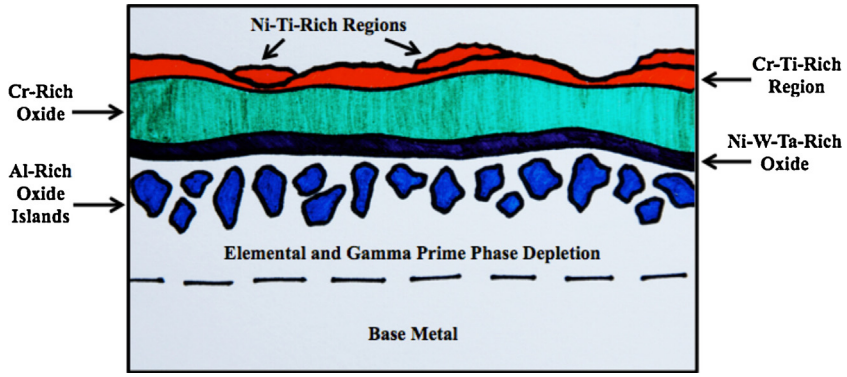

Fig. 5. A schematic model showing the distinct regions of oxides formed in and on GTD111 at 900 °C. The detailed oxide structure, from the top surface down to the base material, was clarified by modelling studies as Ni–Ti oxides, Cr–Ti oxides, Cr_2O_3 oxide band, Ni–W–Ta oxide and finally a blocky Al_2O_3 region.

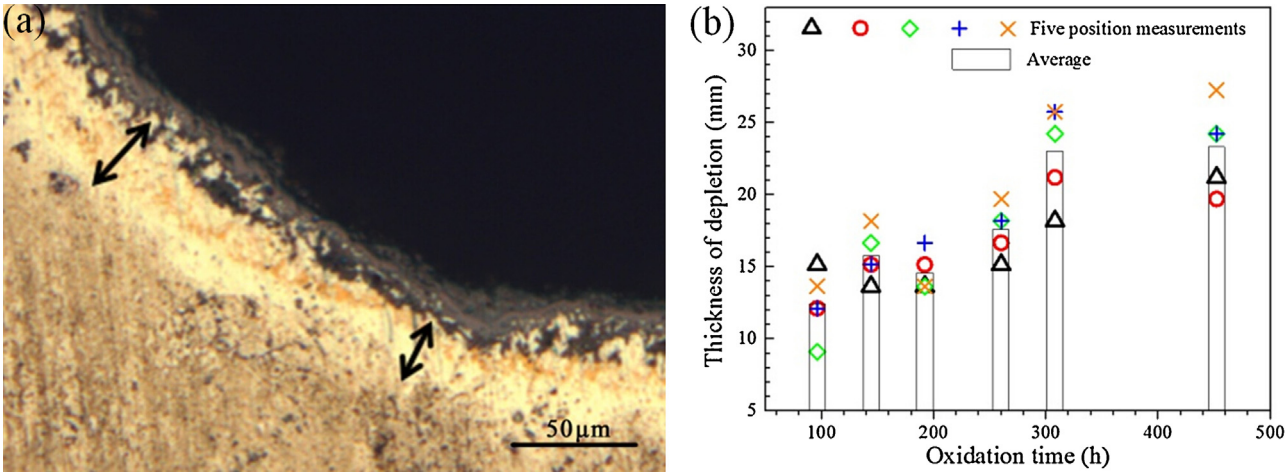

Fig. 7. The gamma prime depletion oxidized for 308 h: (a) optical micrograph, (b) thickness of the depletion with respect to the oxidation time.

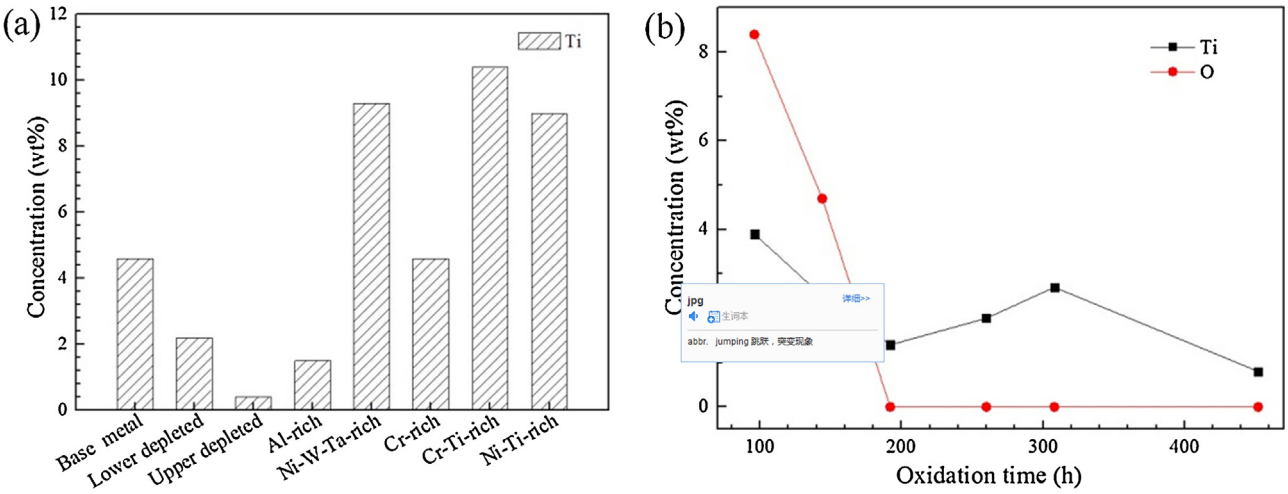

Fig. 8. Migration behavior of Ti during oxidation process at 900 °C: (a) Ti distribution in different oxide regions for 452 h oxidation, (b) Ti and O distribution in the lower depletion with respect to oxidation time.

ever, the overall oxides thickness decreased after 260 h oxidation. It is mostly contributed to that the exterior oxides grew with pores and cracks weakening the scale, and stresses induced by differences in the coefficients of thermal expansion of different oxide scales may have caused the weak oxide regions to spall from the surface, especially during cooling. The thermal expansion coefficients of NiO, Cr_2NiO_4, Cr_2O_3 and Al_2O_3 are respectively as 17.1, 10.0, 8.1 and $8.7 \times 10^{-6}\ K^{-1}$ [8]. Furthermore the oxide layer grew dense after 260 h oxidation, especially for Cr_2O_3 layer.

According to the EDS results, the Al and Ti contents in regions 2 and 3 were lower than that of the base metal, which was associated with the gamma prime phase depletion by the oxidation process. The oxidized sample was depleted of the gamma prime phase near the edges of the surface, as indicated by the bright region in Fig. 7a. It is important to note that the measurements were taken only within the bright region, where the measurement lines beyond the bright region end at the dark scale. Actually the gamma prime phase depletion was composed of regions 2 and 3 (Fig. 3), so it is defined that region 2 is the lower depletion, and region 3 is the upper depletion (Table 3).

Each sample was measured at five positions, as shown in Fig. 7a. The results of this analysis are plotted in Fig. 7b. The testing data were relatively discrete, for the depletion thickness was nonuniform. However, the depletion depth was observed to increase to an average thickness of 23 μm, in general, until 308 h. Very little increase was observed between 308 h and 452 h. It was therefore indicated that the element diffusion rate slowly decrease after 308 h, and on the oxidation rate. The depletion layer growth of GTD111 was different from other oxide layers (Fig. 6) and materials [14].

3.3. Migration behavior of Ti

Fig. 8a shows the depletion of Ti beneath the oxide scale after 452 h oxidation measured using EDS. It is clear that Ti depletion is severe in Cr–Ti and Ni–Ti exterior oxides besides the Ni–W–Ta regions. It is indicated that Ti cations in the material appeared to be constantly moving toward the surface of the sample to react with oxygen in the air. Only trace amounts of Ti were detected in the lower depletion for 452 h oxidation. Fig. 8b presents the concentration change with the oxidation time in the lower depletion. Ti content decreases from 96 h to 192 h by the outward diffusion, but lightly increases until 308 h during the oxidation. This region was not found to be associated with oxygen, as the oxygen did not extend as far into the sample as the variation in Ti concentrations. Correspondingly, the buildup of TiN [19,23,24] particles dispersedly distributes below the Al-rich region changed with the increasing oxidation time from 192 to 308 h, as indicated by the arrows in

Fig. 2c–f. Cracking and spalling of the outer oxides scale results in the nitrogen penetration into the inner oxides scale, and inner nitridation to form TiN occurs, for Ti has a high affinity for nitrogen [25,26]. However, the nitrides particles disappear in lower depletion in the 452 h oxidation samples. Therefore, the formation of continuous Cr_2O_3 oxide layer on GTD111 provides an effective diffusion barrier to reduce the oxidation and inner nitridation rate of those elements, and the thickness of the depletion lightly increase between 308 h and 452 h (Fig. 7b).

3.4. Oxidation mechanisms

The general oxide reaction equation for pure metal is given by:

$$M(s) + 1/2O_2(g) = MO(s) \quad (3)$$

And the two reactants M and O_2 are separated by the solid reaction product MO, as shown by:

$$\begin{matrix} M \\ | \\ \text{Metal} \end{matrix} \Big| \begin{matrix} MO \\ | \\ \text{Oxide} \end{matrix} \Big| \begin{matrix} O_2 \\ | \\ \text{Gas} \end{matrix} \Big| \quad (4)$$

To make the reaction proceed, one or two reactants must pass through the oxide film. Therefore, the reactants transmission through the oxide has been an important part of high temperature oxidation mechanisms [27]. The actual transmission species through the oxide are the electrons and the ions of metal or O_2. There is always either an excess or deficit of metal (or a deficit or excess of oxygen, respectively) ions in the oxide. The resultant relative charge difference in the oxide becomes the driving force for oxidation, and controls the kinetics of the oxidation process. The metal-deficit oxides such as Ni, Cr and Ti oxides grows outward from the surface of the component by the outward diffusion of metal cations to react with oxygen at the oxide/gas interface [28]. On the other hand, the oxygen-deficit or n-type oxides such as Al, W and Ta oxides grows inward from the surface by the diffusion of oxygen anions to react with metal cations at the oxide/metal interface [20].

Based on the above results and discussions, it is verified that the oxidation behavior of GTD111 superalloy is controlled by the diffusions of oxygen, Cr and Ti. Meanwhile, Cr, Al and Ti are all strong oxide formers which have a high affinity for oxygen; they are preferentially oxidized when added to a base metal such as Ni due to the lower free energy of formation [20,29,30]. The oxidation mechanism of GTD111 can be described as follows by a model in Fig. 9. In the first stage (Fig. 9a) the oxygen molecules are adsorbed onto the surface of a specimen. Ti cations with the initial highest mobility allows fast diffusing towards the metal/oxide interface, firstly reacts with O_2, and nuclei of the island Ti-rich oxides forms on the surface as the external oxide for 1 h oxidation. Within the 4 h exposure at 900 °C, a continuous Cr_2O_3 film is quickly formed on the substrate beneath the surface. Simultaneously the oxidation reaction of Al element takes place, which correspond to internal oxidation (Fig. 9b). The initial external oxide scales are more permeable to O^{2-} anions than to metal cations, so that oxygen can easily traverse through these scales [14]. After the initial formation of Al and Cr oxides, Ni and Ti continued to migrate through these regions to form oxide compounds at the surface. Due to the formation of Ti-rich and Cr_2O_3 oxides, solid state reactions occur to form Ni–Ti, Cr–Ti and Ni–Cr spinel phases as parts of the outer oxide layer in the ongoing oxidation stage, which can accelerate the oxidation rate. Ni–W–Ta oxide formed between the Cr_2O_3 band and Al_2O_3 layer, through the inwards diffusion of O^{2-} as the inner oxidation layer, just like Al oxide after approximately 96 h oxidation. However, W and Ta elements inhibit rapid formation of Al_2O_3 because it reduces inward diffusion of oxygen due to their higher valances and larger sizes than Al [8,12–13,15]. For longer exposure times a more compact but still discontinuous Al_2O_3 layer is formed below the Ni–W–Ta oxide layer, which grows in depth (Fig. 9c). Therefore oxidation resistance of GTD111 superalloy was provided by a continuous and dense Cr_2O_3 oxide band, instead of discontinuous Al_2O_3 oxide layer at 900 °C in air.

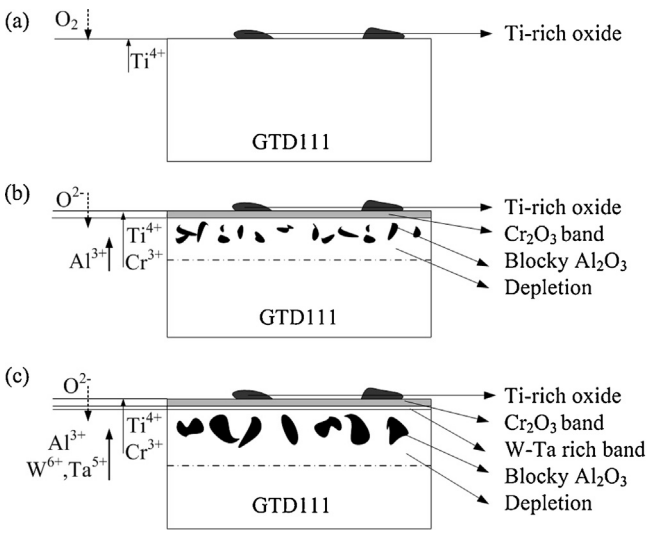

Fig. 9. A schematic model showing the oxidation mechanism of GTD111 at 900 °C: (a) Ti with fast diffusion towards the surface react with O_2 in the initial oxidation stage, (b) a continuous Cr_2O_3 band and blocky Al_2O_3 oxides simultaneously form in the followed oxidation stage, (c) Ni–W–Ta oxide formed between the Cr_2O_3 band and Al_2O_3 layer, through the inwards diffusion in the ongoing oxidation stage.

4. Conclusions

In this paper, the oxidation behavior of GTD111 Ni-based superalloy was studied at 900 °C from 1 h to 452 h. All samples oxidized for 96 h or more times exhibited very similar structures, wherein inconsistent outermost regions high in Ni and Ti were located atop followed by a very dense band high in Cr. Underneath this band of Cr oxide was a thin, continuous band showing concentrations of W–Ta and lesser extents Ti. In all cases, the deepest-forming region was the blocky, discontinuous region high in Al. Cracking and spalling of the outer oxides scale results in the nitrogen penetration into the inner oxides scale, and inner nitridation to form TiN occurs.

A model has been presented for the oxidation mechanisms of GTD111 at 900 °C in air. The first-formed oxide on this alloy was Ti oxide, followed by Cr oxide, Al oxide, and finally the formation of an oxide layer rich in W and Ta. The oxidation resistance of GTD111 superalloy was provided by a continuous and dense Cr_2O_3 oxide band, instead of discontinuous Al_2O_3 oxide layer at 900 °C in air.

Acknowledgements

The research is sponsored by National Natural Science Foundation of China (51375261, 51405258), Tsinghua University Initiative Scientific Research Program (2013Z02-1 2010THZ 02-1), The Specialized Research Fund for Doctoral Program of Higher Education (20130002110009), The Natural Science Foundation of Beijing (3132020).

References

[1] M.Z. Alam, D. Chatterjee, B. Venkataraman, V.K. Varma, D.K. Das, Effect of cyclic oxidation on the tensile behavior of directionally solidified CM-247LC Ni-based superalloy at 87 °C, Mater. Sci. Eng. A 527 (2010) 6211–6218.
[2] R. Pillai, H. Ackermann, H. Hattendorf, S. Richter, Evolution of carbides and chromium depletion profiles during oxidation of Alloy 602CA, Corros. Sci. 75 (2013) 28–37.

[3] F.H. Latief, K. Kakehi, Y. Tashiro, Oxidation behavior characteristics of an aluminized Ni-based single crystal superalloy CM186LC between 900 °C and 1100 °C in air, J. Ind. Eng. Chem. 19 (2013) 1926–1932.
[4] A. Stankowski, Advanced thermochemical cleaning procedures for structural braze repair techniques, Proceedings of ASME Turbo Expo: Power for Land, Sea, and Air, Amsterdam, The Netherlands (2002) 1181–1195.
[5] F. Huang, J. Wang, En-H. Han, W. Ke, Microstructural characteristics of the oxide films formed on Alloy 690 TT in pure and primary water at 325 °C, Corros. Sci. 76 (2013) 52–59.
[6] J. Xiao, N. Prud'homme, N. Li, V. Ji, Influence of humidity on high temperature oxidation of Inconel 600 alloy: oxide layers and residual stress study, Appl. Surf. Sci. 284 (2013) 446–452.
[7] L. Zheng, M. Zhang, J. Dong, Oxidation behavior and mechanism of powder metallurgy Rene95 nickel based superalloy between 800 and 1000 °C, Appl. Surf. Sci. 156 (2010) 7510–7515.
[8] Si. J. Park, S.M. Seo, Y.S. Yoo, Hi-W. Jeong, H.J. Jang, Effects of Al and Ta on the high temperature oxidation of Ni-based superalloys, Corros. Sci. 90 (2015) 305–312.
[9] Y. Wu, T. Narita, Oxidation behavior of the single crystal Ni-based superalloy at 900 °C in air and water vapor, Surf. Coat. Technol. 202 (2007) 140–145.
[10] Y. Wu, T. Narita, The cyclic oxidation behavior of the single crystal TMS-82+ superalloy in humidified air, Mater. Corros. 60 (10) (2009) 781–787.
[11] C.T. Liu, J. Ma, X.F. Sun, Oxidation behavior of a single-crystal Ni-base superalloy between 900 and 1000 °C in air, J. Alloys Compd. 491 (2010) 522–526.
[12] M. Bensch, A. Sato, N. Warnken, E. Affeldt, R.C. Reed, U. Glatzel, Modelling of high temperature oxidation of alumina-forming single-crystal Nickel-base superalloys, Acta Mater. 60 (2012) 5468–5480.
[13] M. Bensch, J. Preußner, R. Hüttner, G. Obigodi, S. Virtanen, J. Gabel, U. Glatzel, Modelling and analysis of the oxidation influence on creep behaviour of thin-walled structures of the single-crystal nickel-base superalloy René N5 at 980 °C, Acta Mater. 58 (2010) 1607–1617.
[14] A. Pfennig, B. Fedelich, Oxidation of single crystal PWA1483 at 950 °C in flowing air, Corros. Sci. 50 (2008) 2484–2492.
[15] A. Sato, Y.-L. Chiu, R.C. Reed, Oxidation of nickel-based single-crystal superalloys for industrial gas turbine applications, Acta Mater. 59 (2011) 225–240.
[16] A. Firouzi, K. Shirvani, The structure and high temperature corrosion performance of medium-thickness aluminide coatings on nickel-based superalloy GTD-111, Corros. Sci. 52 (2010) 3579–3585.
[17] M.D. Trexler, P.M. Sigh, T.H. Sanders Jr, High temperature corrosion behavior of DS GTD-111 in oxidizing and sulfidizing environments, in: Proceedings of the 11th International Symposium on Superalloys, Champion, Pennsylvania, 2008, pp. 699–708.
[18] N. Halem, M. Abrudeanu, G. Petot-Ervas, Al effect in transport properties of nickel oxide and its relevance to the oxidation of nickel, Mater. Sci. Eng. B 176 (2011) 1002–1009.
[19] D.W. Yun, S.M. Seo, H.W. Jeong, Y.S. Yoo, The cyclic oxidation behaviour of Ni-based superalloy GTD-111 with sulphur impurities at 1100 °C, Corros. Sci. 90 (2015) 392–401.
[20] D.A. Jones, Principles and Prevention of Corrosion, 2nd ed., Prentice Hall Press, Upper Saddle River, NJ, 1996.
[21] J.A. Nychka, D.R. Clarke, G.H. Meier, Spallation and transient oxide growth on PWA1484 superalloy, Mater. Sci. Eng. A 490 (2008) 359–368.
[22] L. Zheng, M. Zhang, R. Chellali, J. Dong, Investigations on the growing, cracking and spalling of oxides scales of powder metallurgy Rene95 nickel-based superalloy, Appl. Surf. Sci. 257 (2011) 9762–9767.
[23] S. Cruchley, H.E. Evans, M.P. Taylor, M.C. Hardy, S. Stekovic, Chromia layer growth on a Ni-based superalloy: sub-parabolic kinetics and the role of titanium, Corros. Sci. 75 (2013) 58–66.
[24] G. Gulsoy, G.S. Was, Surface oxidation of Alloy 617 in low oxygen partial pressure He–CO–CO_2 environments at 750–850 °C, Corros. Sci. 90 (2015) 529–534.
[25] U. Krupp, H.-J. Christ, Selective oxidation and internal nitridation during high-temperature exposure of single-crystalline nickel-base superalloys, Metall. Mater. Trans. A 31 (2000) 47–56.
[26] X. Zhong, En-H. Han, X. Wu, Corrosion behavior of Alloy 690 in aerated supercritical water, Corros. Sci. 66 (2013) 369–379.
[27] N. Birks, G.H. Meier, F.S. Pettit, Introduction to the High Temperature Oxidation of Metals, Cambridge University Press, Oxford, 2006.
[28] J. Chapovaloff, F. Rouillard, K. Wolski, M. Pijolat, Kinetics and mechanism of reaction between water vapor, carbon monoxide and a chromia-forming nickel base alloy, Corros. Sci. 69 (2013) 31–42.
[29] L. Liu, Y. Li, F. Wang, The effect of micro-structure on the oxidation behavior of a Ni-based superalloy in water vapor plus oxygen, Mater. Lett. 62 (2008) 4081–4084.
[30] Z. Shi, J. Li, S. Liu, Isothermal oxidation behavior of single crystal superalloy DD6, Trans. Nonferrous Met. Soc. China 22 (2012) 534–538.